IOP Publishing Journal of Physics: Condensed Matter
J. Phys.: Condens. Matter **32** (2020) 225701 (12pp) https://doi.org/10.1088/1361-648X/ab7032

Effects of oxygen variation on the improved structural stability, electronic and optical properties of ZnTeO compounds

Yee Hui Robin Chang[1,2], Tiem Leong Yoon[2], Thong Leng Lim[3], Pin Wai Koh[2] and Eong Sheng Goh[2]

[1] Faculty of Applied Sciences, Sarawak Branch, Universiti Teknologi MARA, 94300 Samarahan, Sarawak, Malaysia
[2] Universiti Sains Malaysia, 11800, USM, Penang, Malaysia
[3] Faculty of Engineering and Technology, Multimedia University, 75450 Melaka, Malaysia

E-mail: robincyh@uitm.edu.my

Received 3 October 2019, revised 13 January 2020
Accepted for publication 27 January 2020
Published 3 March 2020

Abstract

Crystalline ZnTeO thin films are promising materials for next generation photovoltaics. However, their structural stability and optical nonlinearity potential in bulk form have not been reported. Here, structural, electronic and optical properties of ZnTeO composites have been thoroughly studied using genetic algorithm and density functional theory (DFT). Energetically, mechanically and dynamically stable O-rich phases, namely $Zn_2Te_2O_6$ and $ZnTeO_4$, were obtained. Ground-state properties such as lattice constants and simulated XRD were analyzed and compared to the experimental literature wherever possible. With a G_0W_0 corrected band gap, these semiconducting phases display several desirable features, namely, Jahn–Teller distorted cations, hardness and shear anisotropy-induced optical nonlinearity that increase monotonically as O concentration elevates. Such trends appear to be consistent with that seen in the experimental study of ZnTeO thin film. It is observed that Zn-*d*, Te-*p* and O-*p* states have immense influence towards the electronic properties of these structures. Both phases exhibit steep elevation of absorption throughout the ultraviolet (UV) range, hitting peak value of ~5.0×10^5 cm^{-1}. Of particular interest, the non-centrosymmetric $ZnTeO_4$ has second harmonic generation coefficients (9.84 pm V^{-1} and 2.33 pm V^{-1} at static limit) greater than borates crystal and large birefringence that exceeds 0.08 in deep UV region, thus highlighting its potential pedigree as new optical materials in UV range.

Keywords: density functional theory (DFT), electronic properties, linear and nonlinear optics, second harmonic generation (SHG)

S Supplementary material for this article is available online

(Some figures may appear in colour only in the online journal)

1. Introduction

Most semiconductors are comprised of elements that are comparatively well-matched in terms of atom dimensions, ionicity, and electronegativity. Semiconducting materials in this category have energy band gap that can be exactly estimated using a linear interpolation of the end point values, as described by the virtual crystal approximation (VCA) [1]. The VCA model can be altered with an inclusion of quadratic bowing parameter term [2, 3] to suit the application in less well-matched semiconductors. Still, there is a class of semiconductors known as highly mismatched alloys (HMAs), which contain elements with very diverse characteristics. These combinations cannot be accurately expressed using the VCA model [4].

HMAs have over the years emerged as key materials for the application of deep ultraviolet optoelectronics, photovoltaic, harsh environment applications and high-power laser devices [5, 6], mainly due to their ultrawide band gap characteristic and distinctive refractive index of 1.4–2.8 within visible radiation that elevates for shorter wavelengths. To create an HMA, host anions (electronegative metallic anions) are substituted with mismatched anions (isovalent electronegative metallic anions), thus introducing an intermediate band energy level between the valance and conduction band. The composition of mismatched anions will determine the degree of the band structure, or energy gap in short. Initially HMA can only be created through III–V alloys. However, recent advances in thin film technology has made II–VI semiconductors a viable option for the synthesis of HMA [7]. Currently, two most studied HMAs are GaAs doped with N and ZnTe doped with O [8]. These two semiconductors have manifest absorption of sub-bandgap photons, justifying the existence of intermediate band energy level. In II–VI based HMAs, ZnTeO and ZnSeO are of the interest. In the studies of ZnTeO [9–16] and ZnSeO [17, 18], small portion of Te (Se) is replaced with O in dilute oxides, otherwise small fraction of O is replaced with Te (Se) [18–21] in dilute tellurides (selenide) forms.

Interest on ZnTeO arises when it was discovered that ZnTeO-based devices show higher efficiency and photocurrent as compared to ZnTe-based device itself [22]. However, detailed study of their optical nonlinearity potential is extremely lacking. Our literature search also indicates that only one publication on *ab initio* calculations of bulk ZnTeO has been produced so far. Zerroug *et al* [22] used full potential linearized augmented plane wave (FP-LAPW) method as employed in Wien2K to investigate the structural and optical properties of ZnTeO alloys while varying the concentration of oxygen. The calculated static and high-frequency dielectric constants for ZnO and ZnTe end blocks are found to agree reasonably well with the experimental findings. The calculations, nevertheless, were carried out based on the assumption that ZnTeO always maintain the zincblende structure. It must be stressed that local minimum and space group for intermediate oxide ZnTe phases, in premature form, can vary from the pre-conjectured cubic structure. As such, potentially important structures of other symmetries might be missed during the calculation. In our work, we performed a thorough search for whole composition range of oxygen gas within ZnTe-O_2 system, mimicking the influx of O_2 onto ZnTe substance, and compared the formation enthalpy of each fit structure. Being able to characterize efficient 3D optical materials has always been an elusive objective but undeniably important, mainly because of their ability to restrain and regulate EM waves in 3D space [23, 24]. Therefore, findings obtained in our work would conveniently allow researchers or manufacturers to extract instructive data, needed for growing bulk ZnTeO crystals of superior quality by the crystal growth optimization method.

2. Computational method

To identify all probable stable structures in the binary ZnTe-O_2 system, USPEX [25, 26] bound extensive evolutionary calculations that consist of 4–8 atoms, 6–12 atoms, 8–16 atoms and 10–20 atoms sample sizes were performed under atmospheric pressure. Default atom dependent hard constraints such as minimum distance between atoms and minimum volume per block were accessed. In the first generation, 60 random structures with combined number of atoms per unit cell that satisfy the lower-upper limits of sample range and constraints were created. Each structure underwent five relaxation intervals, starting from unrefined to strict conditions, within the framework of density functional theory (DFT) [27, 28] as provided by the Vienna *ab initio* simulation package (VASP) [29, 30]. Reciprocal space resolution of Monkhorst–Pack *k*-meshes was reduced gradually from $2\pi \times 0.15$ Å^{-1} to $2\pi \times 0.07$ Å^{-1}. Methfessel and Paxton scheme with smearing width starting at 0.10 eV and reducing to 0.03 eV was preferred for the relaxation stages.

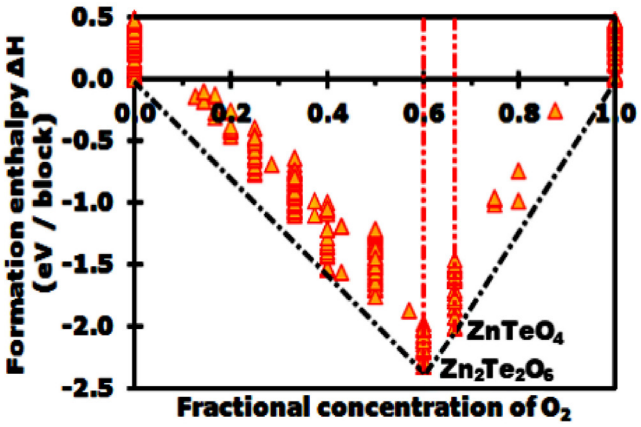

Figure 1. Convex hull for ZnTe-O_2. The lowest free energy of O_2 gas is −5.5953 eV/atom.

We used pseudopotentials with twelve and six apiece valence electrons for Zn ($3d^{10}4s^2$), Te ($5s^25p^4$) and O ($2s^22p^4$), respectively. Enthalpy or DFT computed Gibbs free energy of locally optimized structure was used as fitness, and 60% of lowest-enthalpy structures participated in new structures formation via crossover and mutations techniques, namely the heredity (50%), random (20%), transmutation (10%), softmutation (10%) and lattice mutation (10%) operators. Addition of randomly generated compositions is imperative as it provides a diversity of structures for every generation. Softmutation refers to the induction of structural change by dislodging atoms along the softest mode eigenvectors. In lattice mutation, lattice vectors of the parent structure are changed by applying a symmetric strain matrix. This operator helps to minimize events of untimely convergence towards a particular lattice. Transmutation turns randomly chosen atoms within a parent structure into other chemical species present in it. Each newly formed offspring was again compared to preset hard restrictions, relaxed and moved into the next generation if survived. Bad candidates with quality aspect determined by the enthalpy value were eliminated. The above cycle was repeated until generation number 50. At this stage, selected low enthalpy individuals have been fully relaxed.

Selected stable and metastable phases were reoptimized with increased precision using a fully automatic $4 \times 4 \times 4$ *k*-point grid Monkhorst–Pack scheme in a static self-consistent run,

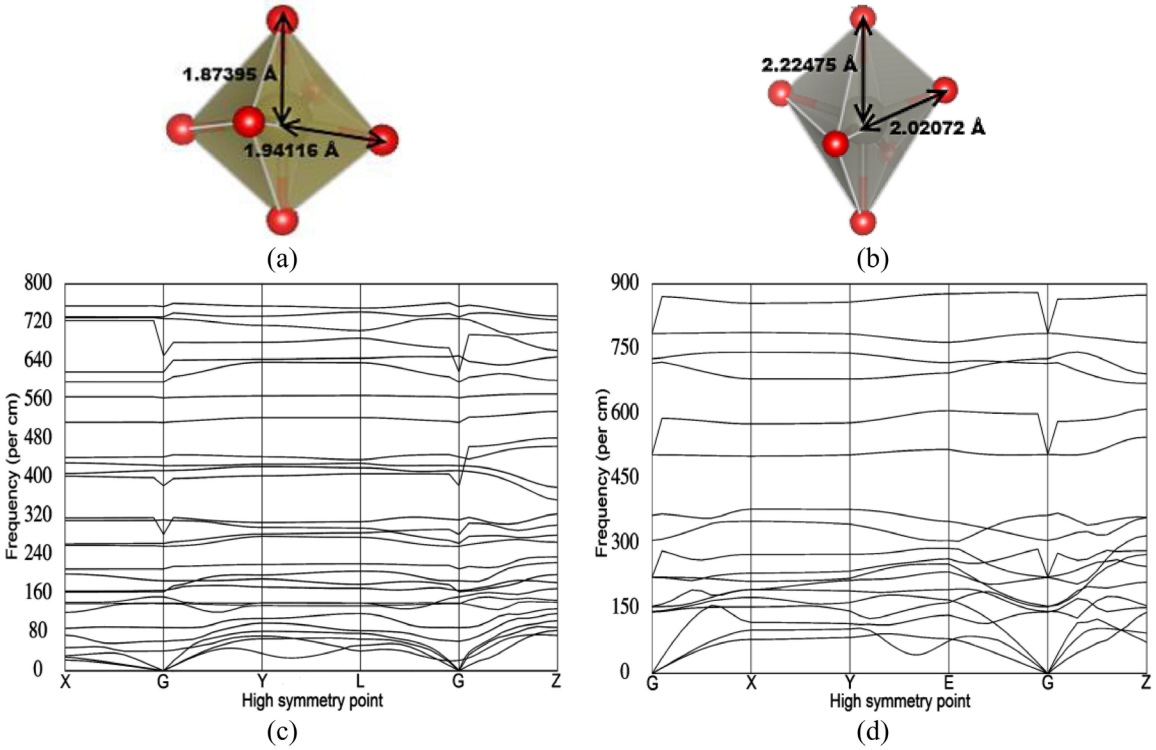

Figure 2. Octahedral framework of (a) $[TeO_6]$ and (b) $[ZnO_6]$ units. Phonon dispersion plots of $Zn_2Te_2O_6$ and $ZnTeO_4$ are represented by (c) and (d).

re-relaxing the ionic positions. The electronic relaxation stopped when force between atoms and energy change per atom were below 1×10^{-4} eV Å^{-1} and 1×10^{-5} eV, respectively. The calculation of the electronic properties was performed using generalized gradient approximation (GGA) of Perdew–Burke–Ernzerhof (PBE) [31] furnished by VASP, in terms of exchange correlation (*XC*) potentials. Effects of core electrons on valence orbitals were described using projector-augmented wave approach, with plane-wave threshold kinetic energy chosen as 350 eV. Tetrahedron method with Blöchl corrections was utilized in all cases. For the computations of G_0W_0 and linear and nonlinear optical parameters, we employed DFPT [32] as implemented in the ABINIT [33, 34] code, in which norm-conserving pseudopotentials and PBE-GGA [35] exchange-correlation functional were preferred. To avoid having symmetric atomic positions and lattice tolerance inconsistencies that might arise due to different codes, we reoptimized again every study specimen using ABINIT, before executing density functional perturbation theory (DFPT) calculations. Convergence studies indicate that a cutoff of 35 Hartree and $4 \times 4 \times 4$ *k*-point meshes were enough to produce convergence in energy. Number of unoccupied states equivalent to twice the strict minimum ($0.5 \times$ total valence electron per unit cell), 35 Hartree cut-off energy and denser *k*-point grids of $12 \times 12 \times 12$ were applied for optical run.

3. Results and discussion

3.1. Structural properties

Towards the end of structural prediction, formation enthalpy (ΔH_{ZnTeO}) of fittest structures was plotted against *y*, O_2 composition. Formation enthalpy of ZnTe-O_2 was evaluated using

$$\Delta H_{ZnTeO} = [E_{ZnTeO} - [xE_{ZnTe} + yE_O]] / (x + y). \quad (1)$$

A specific structure is classified as energetically stable if it fulfils the following two principles: (1) being a ground state structure with negative formation enthalpy and (2) is close to the lowest lying composition. Figure 1 illustrates the convex hulls of the ZnTeO composites at barometric pressure. It comprises of points that commensurate to phases with the lowest formation enthalpy at exact compositions, in reference to the lowest enthalpy structures of base elements. The perforated line joining all phases with the lowest negative formation enthalpies is termed as a convex hull. As can be seen, global minimum structure or composite with lower Gibbs free energy than any phase accumulation is the triclinic $P\bar{1}$ $Zn_2Te_2O_6$ compound. Tetragonal $I\bar{4}m2$ $ZnTeO_4$ was projected as the nearest metastable phase to lowest ground state structure, with approximately 0.05 eV per atom difference between them. Their geometries were added as seeds for further fixed composition calculations, with greater percentage of mutations used as offspring generator. Output produced is consistent with variable composition runs, hence ensuring acquisition of well-relaxed specimens.

Their dynamical stability is confirmed by analyzing the phonon spectrum within whole Brillouin zone in figure 2, where no negative frequencies are observed. The $I\bar{4}m2$ structure exhibits an ordered 3D linkage comprised of $[ZnO_6]$ and $[TeO_6]$ octahedra. Careful analyses at these units point to incidence of elongated and compressed distortions (see figure 2). End block structure of binary ZnTe was correctly forecasted to adopt a

Table 1. Crystallographic data of fit ZnTeO. Grey, yellow and red denote the Zn, Te and O atoms, respectively. Haynes and Kittel [36, 37] give the experimental values of lattice constants for ZnTe.

Phase	Unit cell	Lattice constants/Å			Atomic Wyckoff positions
		a	*b*	*c*	
$ZnTeO_4$	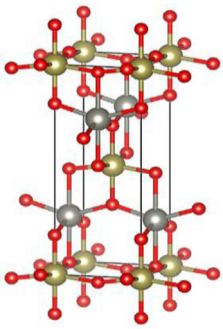	3.8435	3.8435	9.9944	Zn 2d (0.000 00, 0.500 00, 0.750 00) O 4e (0.000 00, 0.000 00, 0.187 50) O 4f (0.000 00, 0.500 00, −0.027 40) Te 2a (0.0000, 0.0000, 0.0000)
$Zn_2Te_2O_6$	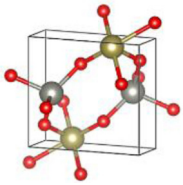	5.4040	5.2280	5.0360	Zn 2i (0.238 21, −0.171 76, −0.483 40) O 2i (−0.116 84, −0.176 38, −0.374 46) O 2i (−0.401 27, 0.083 23, 0.183 39) O 2i (0.402 38, −0.411 83, 0.240 24) Te 2i (0.301 77, 0.289 32, 0.057 10)
Zn_2Te_2	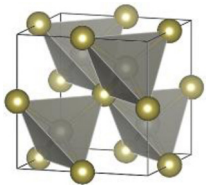	6.0345 6.1010	6.0345 6.1010	6.0345 6.1010 [36]	Zn 4d (0.750 00, 0.750 00, 0.750 00) Te 4b (0.500 00, 0.500 00, 0.500 00)
Zn_6Te_6	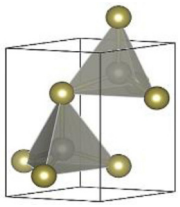	4.2337 4.2700	4.2337 4.2700	6.9670 6.9900 [37]	Zn 2b (0.333 33, 0.666 67, −0.188 91) Te 2b (0.333 33, 0.666 67, 0.184 38)

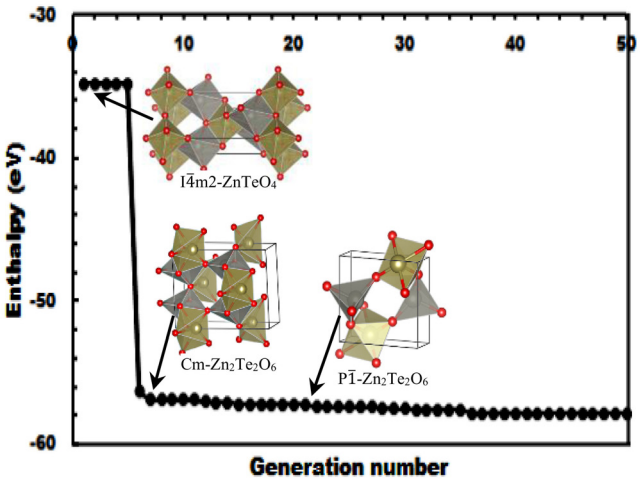

Figure 3. Enthalpy of the best individual versus generation number. Average population size of 30.

zincblende form [36], which transforms to wurtzite layout [37] at slightly higher formation enthalpy. Table 1 summarizes the crystallographic data of aforementioned four phases. Note that the computed physical dimension of Zn_2Te_2 and Zn_6Te_6 unit cells are extremely close to experimental values [36, 37]. Moreover, the calculated powder pattern (see supplementary figure 1 (stacks.iop.org/CM/32/225701/mmedia)) for cubic Zn_2Te_2 also resembles actual XRD analysis [38], thus ensuring the reliability of our applied methodology. Reproduction of experimentally grown $ZnTeO_3$ and $Zn_2Te_3O_8$ [39] phases was not detected. Absence of $ZnTeO_3$ and $Zn_2Te_3O_8$ is also reported in the work by Nabetani *et al* [40].

The proficiency of the USPEX algorithm in yielding various energetically stable structures is extremely efficient, to which in our adopted input setting only between 30–200 structures (figure 3) were calculated before the metastable $ZnTeO_4$ and pre-global minimum $Zn_2Te_2O_6$ phases started appearing. Note that the best $Zn_2Te_2O_6$ structure underwent a monoclinic to triclinic transition in the 22th generation. Its structure and energy remained constant after the 35th generation.

3.2. Electronic properties

Having examined the primitive cells and energetics of numerous ZnTe-O_2 stoichiometries, we now shift to their electronic properties. Figure 4 shows the total and projected

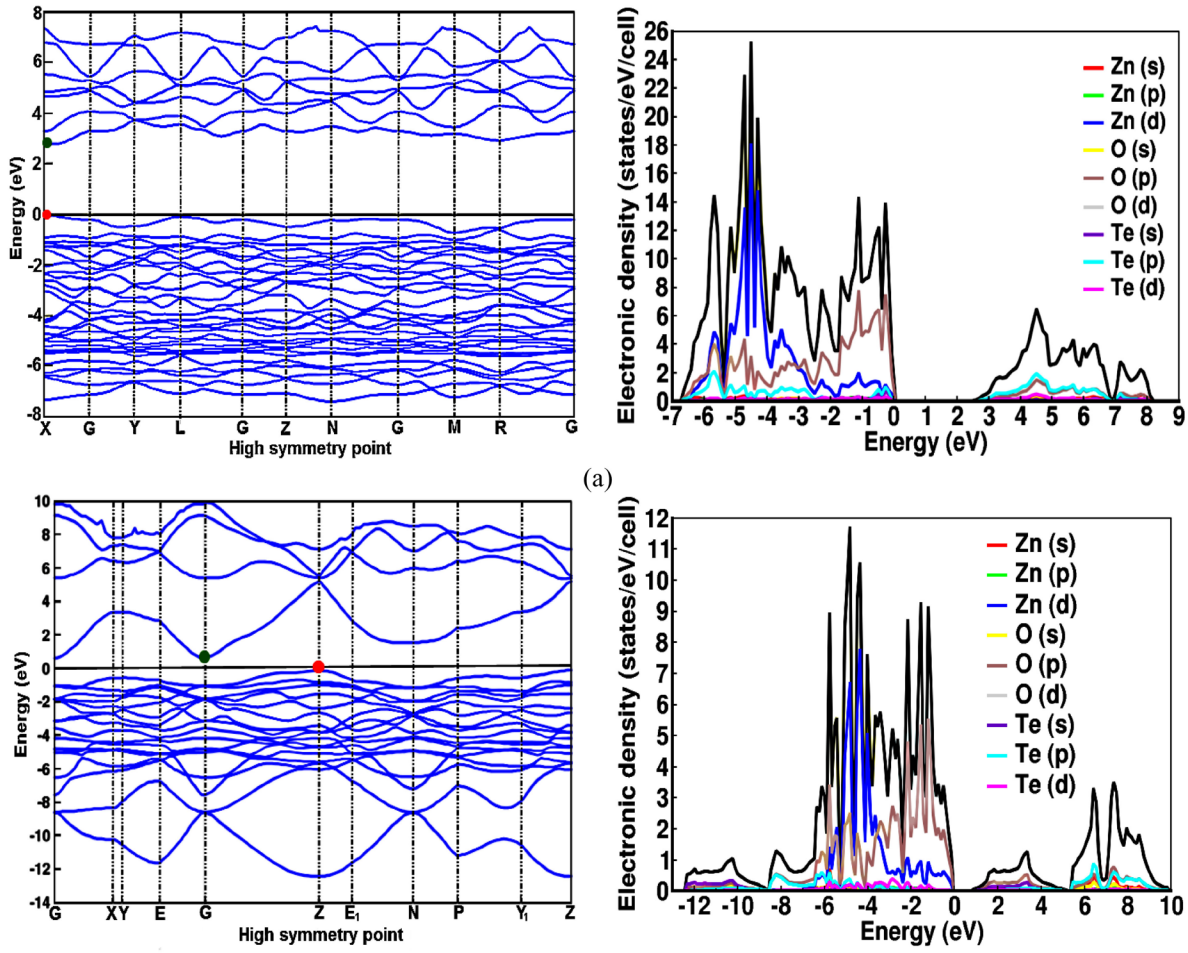

Figure 4. Electronic band structure and projected DOS for (a) $Zn_2Te_2O_6$ and (b) $ZnTeO_4$ whereby green and red spheres represent the CBM and VBM, correspondingly.

Table 2. Computed KS and G_0W_0 energy gap (eV) for $Zn_2Te_2O_6$ and $ZnTeO_4$.

	$Zn_2Te_2O_6$	$ZnTeO_4$	
	X	Z	$Z \rightarrow \Gamma$
KS	2.86	5.40	0.74
G_0W_0	4.27	7.25	2.59

density of states (PDOS) for all ground-state composites. It is clearly depicted that their respective PDOS are made up of three pronounced energy regions: (1) an overlapped Zn-*d*/O-*p* and Te-*p*/O-*p* states in the deeper lying valence band (from −2.0 to −7.0 eV for $Zn_2Te_2O_6$, from −3.0 to −9.0 eV for $ZnTeO_4$), (2) localized Zn-*d* band and (3) a segregated conduction band. The first band is densely occupied by the Zn-*d* orbitals, with contributions from *p* orbitals of O and Te atoms. Hence, the influence of this band to the bonding is extremely strong. Subsequent upper valence band is a result of weaker hybridization from the *d* and *p* states of Zn and O atoms. Addition of O atoms leads to the introduction of localized states, which subsequently go through a reciprocal action with delocalized states of ZnTe host crystal. This interaction is responsible for the splitting of conduction band (located at ~7.0 eV and ~5.5 eV of figures 4(a) and (b)), a unique feature of most HMAs.

Sharp dissimilarity between their PDOS plots indicate a strong dependence on O composition. In contrast, $ZnTeO_4$ appears to have a broader but lower peak plot, prompting a wider range of atomic orbitals hybridization. Covalency is enhanced under these circumstances. We solidified this claim by exploiting Lyakhov–Oganov [41] model (http://han.ess.sunysb.edu/hardness/), which engages bond strengths and bond topology for hardness calculation. Calculated hardness of $Zn_2Te_2O_6$ and $ZnTeO_4$ are 3.722 GPa and 6.828 GPa, thereby suggesting a positive correlation of covalency with O content. Band diagrams in figure 4 imply a direct and indirect energy gap nature for $Zn_2Te_2O_6$ and $ZnTeO_4$ phases, with maximum-minimal energy states at X and $Z \rightarrow \Gamma$, respectively. The Kohn–Sham (KS) and single-shot G_0W_0 corrected eigenvalues are listed in table 2.

The direct energy difference between conduction band minimum (CBM) and valence band maximum (VBM) appears to widen as O concentration rises. A similar trend has also been reported by Yu *et al* [9] in their work about ZnTeO preparation via insertion of O into ZnTe host alloy. Compounds with such high energy band gap have been projected in certain studies

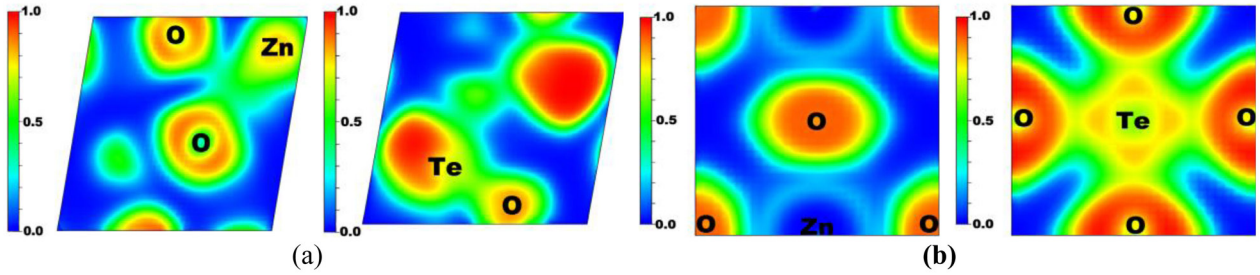

Figure 5. The calculated ELF of (a) triclinic $Zn_2Te_2O_6$ and (b) tetragonal $ZnTeO_4$ phases.

Table 3. Elastic constants (GPa) for ZnTe-O_2.

	C_{ij}								
Phase	C_{11}	C_{12}	C_{13}	C_{22}	C_{23}	C_{33}	C_{44}	C_{55}	C_{66}
$Zn_2Te_2O_6$	238.72	105.63	107.89	201.95	106.76	107.89	205.27	102.31	87.68
$ZnTeO_4$	317.79	128.97	116.74	308.80	128.16	116.74	257.80	140.07	126.25

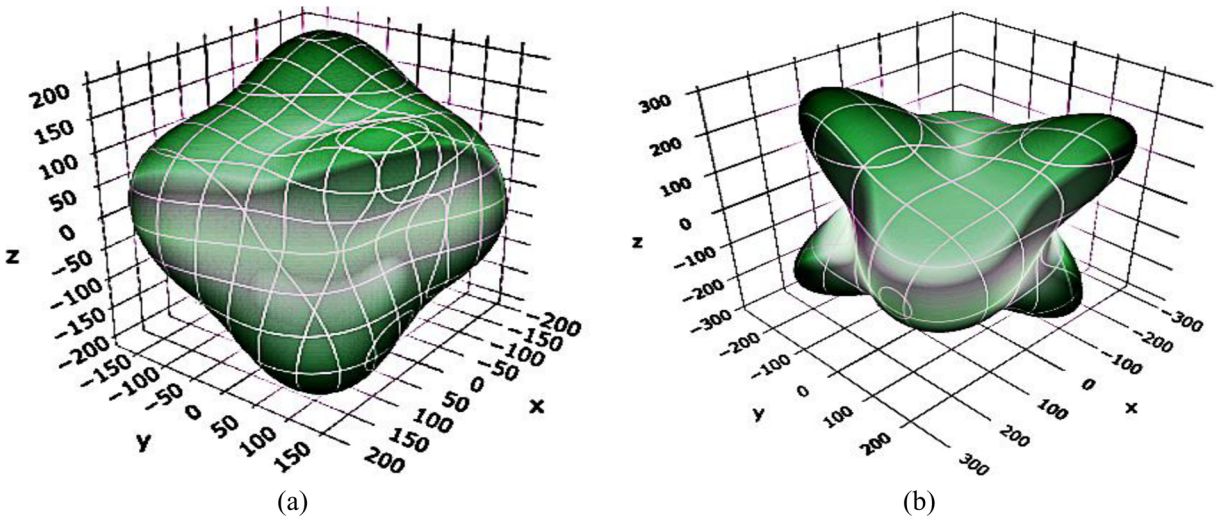

Figure 6. 3D contour plot of Young's modulus.

[42, 43] to exhibit a high level of laser damage threshold. During second harmonic generation (SHG) process, certain amount of SHG signals generated may have energy greater than the band gap of nonlinear optical (NLO) crystal. This results in the production of point defects in the crystal and yields more energy level to the atoms, thus causing optical absorption at definite wavelengths (color center). The increase of absorption at SHG wavelength often leads to crystal damage. As such, materials with large band gap are desired candidates for SHG purpose.

We include herewith (figure 5) the electron localization function (ELF) to comprehend the bonding nature in $Zn_2Te_2O_6$ and $ZnTeO_4$ structures. The estimated ELF of ~0.5 for Zn–O and Te–O bonds in triclinic structure corresponds to weak chemical interactions. A different scenario is noted in tetragonal structure, where its higher estimated ELF (~0.75) for Te–O bonds signifies an enhanced covalent bonding.

3.3. Optical nonlinearity enhancement via elastic anisotropy

The elastic parameters of a substance are measurable through its reaction to external stress. Contrarywise, the applied stress is mandatory in maintaining specific deformation, and can be used to examine elastic properties that directly quantify the mechanical stability. The computed elastic constants for all predicted stable ZnTeO compounds are stored in table 3. These compounds are deemed having sufficient mechanical stability if the following stability criteria [44, 45] are satisfied:

$$\text{Tetragonal} \rightarrow C_{11} > |C_{12}|, 2C_{13}^2 < C_{33}(C_{11}+C_{12}), C_{44} > 0, C_{66} > 0$$

$$\text{Triclinic} \rightarrow \begin{vmatrix} C_{11} & \cdots & C_{16} \\ \vdots & \ddots & \vdots \\ C_{61} & \cdots & C_{66} \end{vmatrix} > 0.$$

By substituting the elastic parameters in table 3 into above corresponding inequalities, we noticed that all predicted phases satisfy the stability requirements, hence confirming sufficient

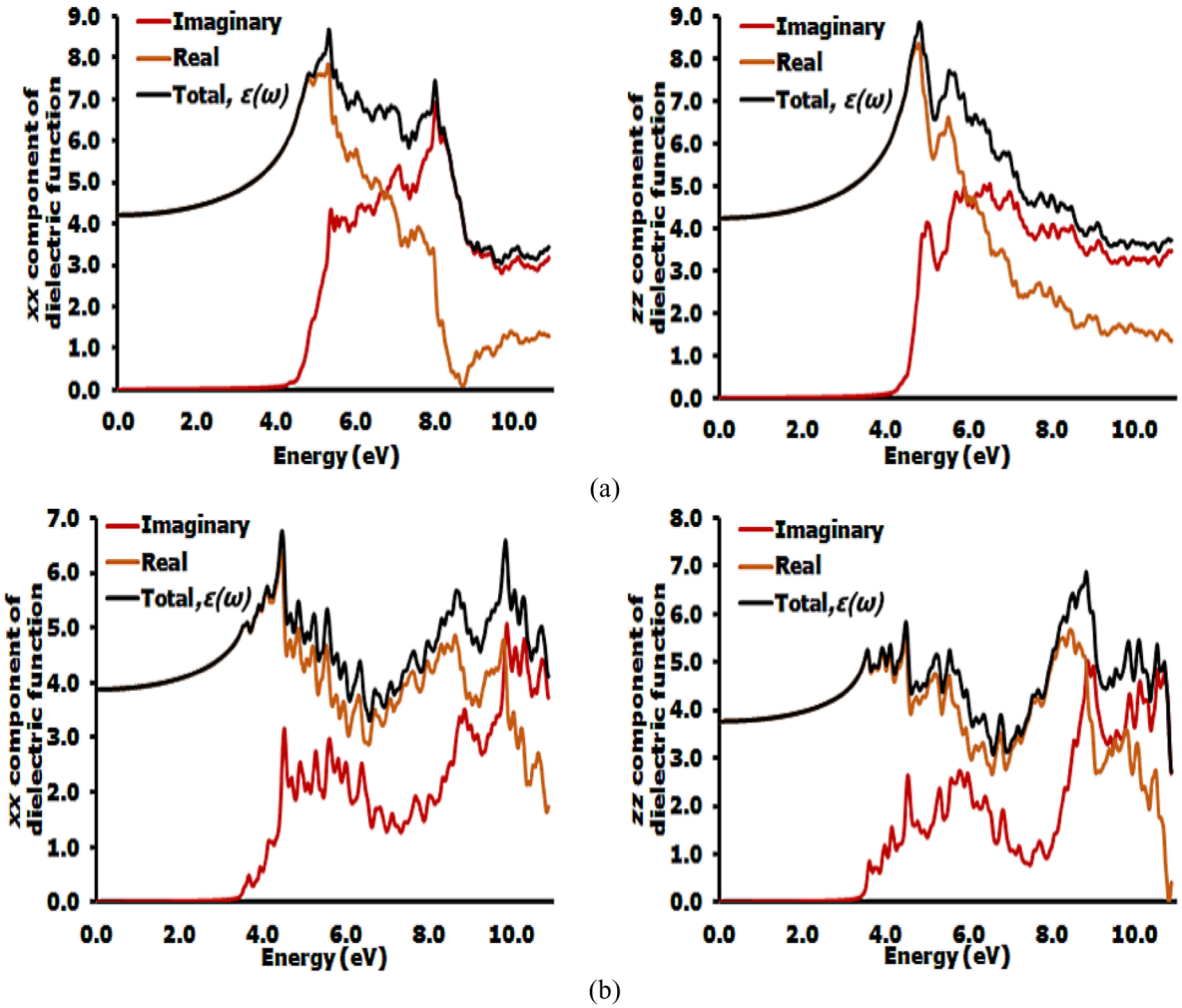

Figure 7. Dielectric functions for (a) $Zn_2Te_2O_6$ and (b) $ZnTeO_4$.

mechanical stability in each of them. The values of C_{11}, C_{22} and C_{33} for both phases are quite uneven and as a result events of disproportionate atomic bonding strength along [1 0 0], [0 1 0] and [0 0 1] directions will be apparent. This occurrence is indicative of a high elastic anisotropy degree, a promising condition for the enhancement of optical nonlinearity.

Along the way, we performed the tensors analysis (see supplementary table 1) via online tool ELATE [46]. Their computed Poisson's ratio ν of 0.2808 and 0.2565 for $Zn_2Te_2O_6$ and $ZnTeO_4$ means both phases are of ceramic class [47]. The ν below 0.26 indicates greater covalency [48] in $ZnTeO_4$ phase, which explains its lower but wider DOS and higher computed hardness. 3D plot of their respective Young's modulus further signifies presence of high anisotropic behavior, particularly $ZnTeO_4$ phase, as illustrated by the notable spherical shape deformation in figure 6. The universal anisotropy value [49] and percent of anisotropy were also calculated and used to quantify evidence of anisotropy:

$$A^U = 5\frac{G_{\text{Voigt}}}{G_{\text{Reuss}}} + \frac{B_{\text{Voigt}}}{B_{\text{Reuss}}} - 6 \tag{2}$$

$$A_B = \frac{B_{\text{Voigt}} - B_{\text{Reuss}}}{B_{\text{Voigt}} + B_{\text{Reuss}}} \tag{3}$$

$$A_G = \frac{G_{\text{Voigt}} - G_{\text{Reuss}}}{G_{\text{Voigt}} + G_{\text{Reuss}}}. \tag{4}$$

A^U index is a reliable indicator that furnishes consistent results for elastic anisotropy events in most compounds. Degree of anisotropy is proportional to the deviation of A^U from zero. One can interpret that the A^U value of 0.7498 and 0.9743 hint at high elastic anisotropy in $Zn_2Te_2O_6$ and $ZnTeO_4$ crystalline structures. Both $Zn_2Te_2O_6$ and $ZnTeO_4$ have lower A^B value (1.11% and 0.75%) in contrast to their A^G (6.78% and 8.75%), which means origin of optical nonlinearity is instigated by anisotropy of shear modulus. This finding suggests that there could be a positive inclination of overall ZnTeO anisotropy nature towards oxygen content. This kind of elastic anisotropy has also been reported to trigger various anisotropic photophysical properties that promote strong optical anisotropy [50].

3.4. Optical properties

Electronic band structure and energy gap play a pivotal role in determining the complex dielectric function $\varepsilon(\omega)$ of semiconducting materials. As such, gap difference between KS and G_0W_0 was included to make the following optical spectrum

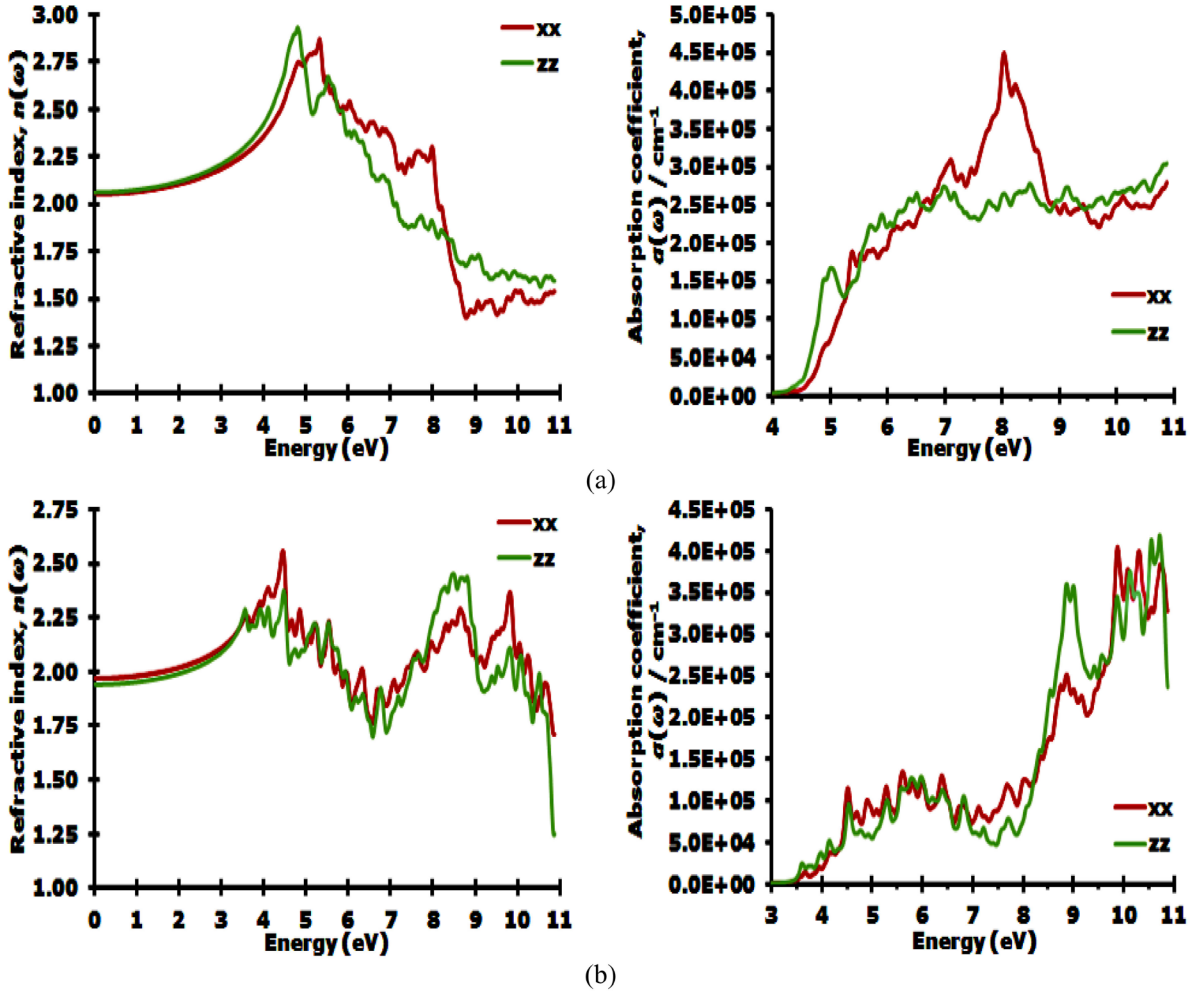

Figure 8. $n(\omega)$ and $\alpha(\omega)$ for (a) $Zn_2Te_2O_6$ and (b) $ZnTeO_4$.

computations more realistic. Linear optical response in our work was calculated using random-phase approximation (RPA) [51] within the frame of DFT, describing the interband transitions at absorption region. Omission of indirect intraband transitions which are associated to free carrier absorption involving phonons scattering is a reasonable approach since both $Zn_2Te_2O_6$ and $ZnTeO_4$ phases are ultra-wide band gap materials. For any study specimen, $\varepsilon(\omega) = \varepsilon_1(\omega) + i\varepsilon_2(\omega)$ as a function of incident photon energy is composed of real and imaginary parts. Real component $\varepsilon_1(\omega)$, which is associated with electronic polarizability, can be estimated from its imaginary counterpart $\varepsilon_2(\omega)$ via Kramers–Kronig transformation of imaginary part $\varepsilon_2(\omega)$. We computed the imaginary part of dielectric function from RPA, where complex dielectric function $\varepsilon(\omega) = 1 + 4\pi\chi^{(1)}(-\omega, \omega)$. Summating the transitions from occupied to unoccupied states over the entire Brillouin zone generates $\varepsilon_2(\omega)$. The linear optical susceptibility $\chi^{(1)}$ was scissor corrected by a magnitude corresponding to the difference between the KS band gap and *GW* corrected band gap, in an effort to include the many-body effects or self-energy effects. The same scissor approximation was also applied to the calculations of effective second-order susceptibility tensor $\chi^{(2)}$. Equations denoting $\chi^{(1)}$ and $\chi^{(2)}$ are as follows:

$$\chi^{(1)}_{xy}(-\omega, \omega) = \frac{e^2}{\Omega\hbar}\sum_{nmk} f_{nm}(\boldsymbol{k})\frac{r^a_{nm}(\boldsymbol{k})\, r^b_{mn}(\boldsymbol{k})}{\omega_{mn}(\boldsymbol{k}) - \omega + \frac{\Delta}{\hbar}(\delta_{mc} - \delta_{nc})} \tag{5}$$

$$\chi^{(2)}(-2\omega, \omega, \omega) = \chi^{(2)}_{xyz}(-2\omega, \omega, \omega) + i\frac{\sigma^{(2)}_{xyz}(-2\omega, \omega, \omega)}{2\omega} \tag{6}$$

where Ω, r_{nm}, c and Δ indicate unit cell volume, elements of momentum matrix in k space, conduction states and energy shift, respectively. Subscript letters x, y and z designate the Cartesian components. The first and second terms in (6) represent the pure interband influence and contribution of the susceptibility resulting from the modification of the intraband motion by the polarization energy associated with the interband motion, as described below:

$$\chi^{(2)}_{\text{inter}}(2\omega, \omega, \omega) = \frac{1}{\Omega}\sum_{nmlk} W_k \times \left\{\frac{2r^a_{nm}\left(r^b_{ml}r^c_{\ln}\right)}{(\omega_{lm} - \omega_{ml})(\omega_{mn} - 2\omega)} - \frac{1}{(\omega_{mn} - \omega)}\left[\frac{r^c_{lm}\left(r^a_{mn}r^b_{nl}\right)}{(\omega_{nl} - \omega_{mn})} - \frac{r^b_{nl}\left(r^c_{lm}r^a_{mn}\right)}{(\omega_{lm} - \omega_{mn})}\right]\right\} \tag{7}$$

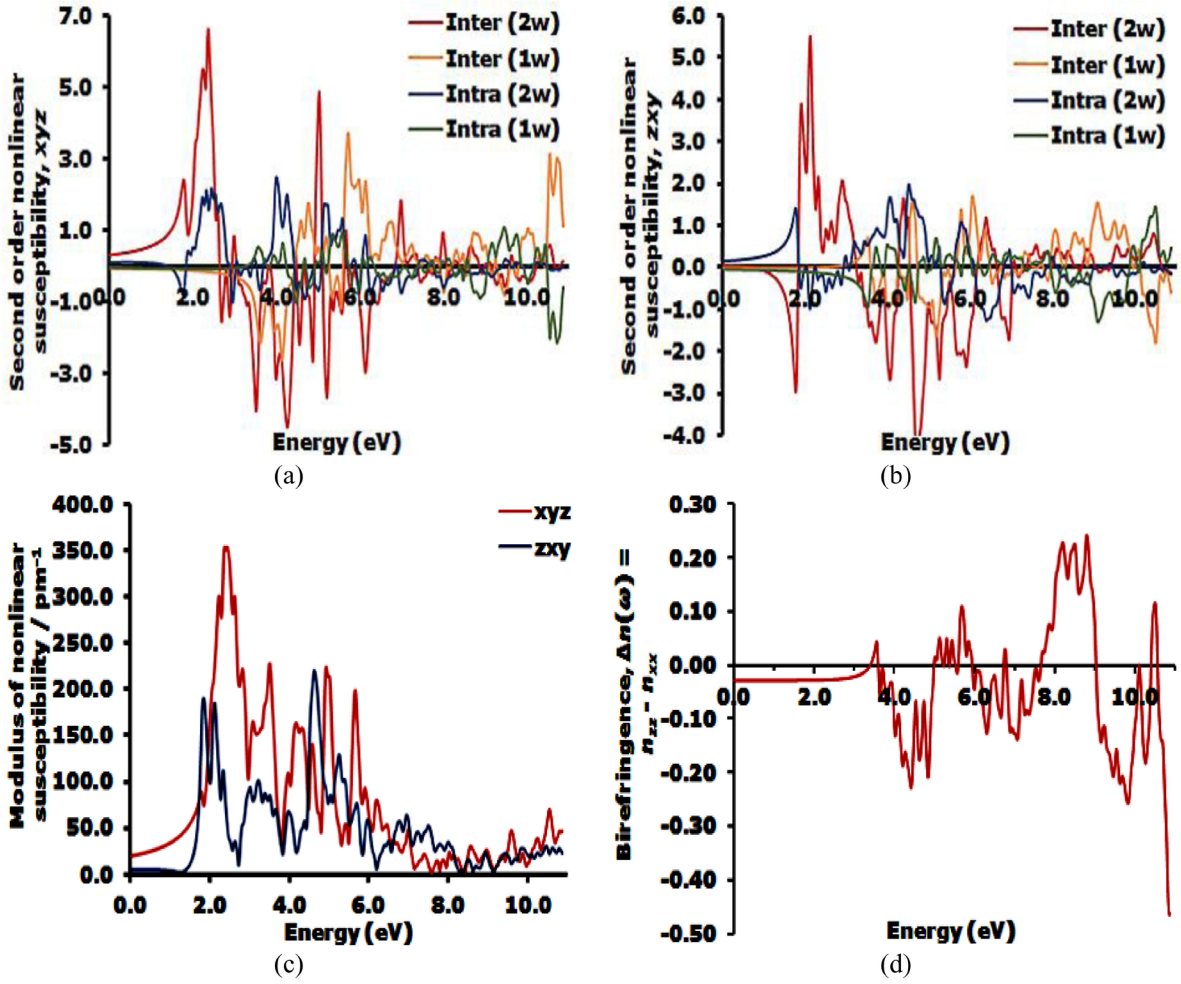

Figure 9. Calculated (a) *xyz* and (b) *zxy* components of nonlinear susceptibility, (c) modulus of $\chi^{(2)}$ and (d) birefringence $\Delta n(\omega)$ for $ZnTeO_4$.

$$\chi^{(2)}_{\text{mod}}\ (2\omega,\omega,\omega) = \frac{1}{2\Omega}\sum_{k} W_k \left\{ \sum_{nml} \frac{1}{\omega^2_{mn}(\omega_{mn}-\omega)} \times \left[\omega_{nl} r^a_{lm}\left(r^b_{mn} r^c_{nl}\right) - \omega_{lm} r^a_{nl}\left(r^b_{lm} r^c_{mn}\right)\right] - i\sum_{nm} \frac{r^a_{nm}\left(r^b_{mn}\Delta^c_{mn}\right)}{\omega^2_{mn}(\omega_{mn}-\omega)} \right\} \tag{8}$$

where n, m, l and W_k indicate the valence states, conduction states, all states and k-point weightage. The momentum matrix elements r_{nm} are determined by response wavefunction, which is computed via DFPT. The basis of the amended linear susceptibility is originating from an improved Hamiltonian, which has accounted a k independent energy shift, projected on top of the conduction states. A detailed derivation of equation (5) and specific terms in (6) have been presented in the work by Sipe *et al* [52] in their work on independent-particle approximation.

These fundamental properties can then be used to calculate optical spectra such as refractive index $n(\omega)$ and absorption coefficient $\alpha(\omega)$. Detailed descriptions of their calculations are listed in our earlier works [53, 54]. As triclinic and tetragonal crystal classes have different nonzero linear susceptibility, for clarity, we consider the *xx* and *zz* elements. The computed dielectric functions for $Zn_2Te_2O_6$ and $ZnTeO_4$ are displayed in figure 7, separately. We notice that $ZnTeO_4$ with higher O proportion has a more drastic distortion to its $\varepsilon_1(\omega)$ and $\varepsilon_2(\omega)$ curves, as demonstrated by the greater number of dominant peaks formed. From the calculated PDOS in figure 4, we note that the peaks for imaginary part $\varepsilon_2(\omega)$ of $ZnTeO_4$ below 4 eV are assigned to the $5s \rightarrow 2p$ transitions while the unoccupied $5p$ bands begin after 4 eV. Peaks above 5 eV are attributed to $2s \rightarrow 5p$, $4s \rightarrow 5p$ and $2p \rightarrow 5p$ transitions. In contrast, the peaks for imaginary part $\varepsilon_2(\omega)$ of $Zn_2Te_2O_6$ are merely ascribed to $2p \rightarrow 5p$ and $4s \rightarrow 2p$ transitions, hence contributing to smaller number of dominant peak structures in $Zn_2Te_2O_6$ phase. Average static dielectric constant, $\varepsilon(0) = [\varepsilon_{xx}(0) + \varepsilon_{yy}(0) + \varepsilon_{zz}(0)]/3$, decreases from 4.295 to 3.840 as direct band gap increases from 4.265 eV to 7.246 eV. This trend is well described by the Penn model [55], in which $\varepsilon(0) \propto 1/(\text{band gap})^2$.

Figure 8 illustrates the dispersion curves of $n(\omega)$ and $\alpha(\omega)$ for ZnTe-O_2 alloys. Mean zero-limit refractive index, $n(0) = [n_{xx}(0) + n_{yy}(0) + n_{zz}(0)]/3$, declines from 2.055 to 1.960 during triclinic to tetragonal transition. Biaxial and uniaxial birefringence are seen in both crystals, and the distinct refractive indices become prominent in the UV region.

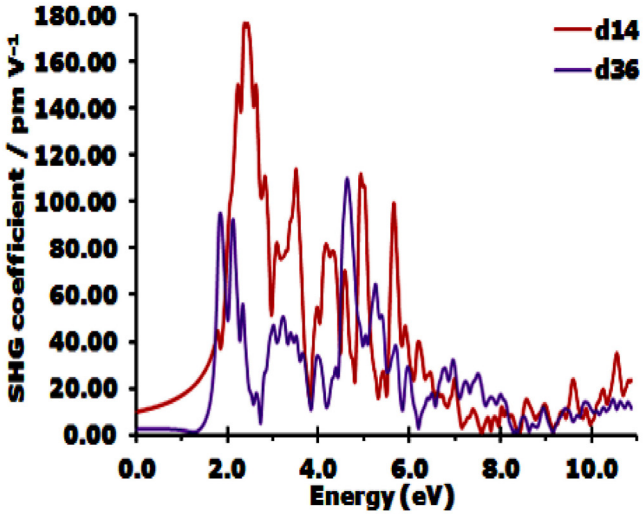

Figure 10. Calculated nonzero SHG coefficients for $ZnTeO_4$.

It has been a well-known fact that birefringence is one of the catalysts for interesting NLO behaviors [56]. Absorption coefficient of triclinic $Zn_2Te_2O_6$ starts increasing as light wavelength decreases approaching its band gap, with consistent increase that reaches values of $\alpha > 10^5$ cm^{-1} in UV range. In the case of tetragonal $ZnTeO_4$, a substantially increased absorption first occurs at its indirect band gap edge, while a steeper increase emerges at the direct band gap point and is extended till deep UV region. The observed high absorption in UV span means these materials are potential candidates for UV trapping system, which uses UV radiation to generate electricity but permits visible light transmission. This wide coverage in UV region also demonstrates the suitability of bulk ZnTeO as host materials for UV-pumped phosphor. $Zn_2Te_2O_6$ and $ZnTeO_4$ fall under the crystal class of $\bar{1}$ and $\bar{4}$ 2m, correspondingly. Due to the influence of Kleinman symmetry [57], nonlinear tensor elements in $Zn_2Te_2O_6$ cease to exist while $ZnTeO_4$ has two categories of independent non-vanishing SHG coefficients. These include $d_{14} = d_{25}$ and d_{36}.

Birefringence $\Delta n(\omega)$, imaginary second order susceptibilities and absolute values of *xyz* and *zxy* components are portrayed in figure 9. Birefringence is an important criterion in determining efficient NLO materials because of its strong correlation with phase-matchability, a phenomenon essential for effective nonlinear interaction. It is noteworthy that $ZnTeO_4$ has reasonably high birefringence (Δn greatly surpasses 0.08) [58–60] that changes alternately between positive to negative values in the entire UV zone, suggesting its versatility to adopt either quartz and ice or calcite behaviors. The palpable conflicting values of inter/intraband for 2ω and ω resonances gives indication there is considerable enhancement in the anisotropy between $\chi^{(2)}_{xyz}$ and $\chi^{(2)}_{zxy}$ tensor components when going from the linear optical properties to the nonlinear optical properties. Overall, $\chi^{(2)}_{xyz}$ is the dominant tensor component, as indicated by its static limit SHG tensor of 19.68 pm V^{-1} whereas $\left|\chi^{(2)}_{zxy}(0)\right| = 4.65$ pm V^{-1}.

The computed d_{14} and d_{36} ($0.5\times$ modulus of SHG tensor) in figure 10 range from 9.84–2.34 pm V^{-1} and 2.33–1.13 pm V^{-1}, spanning the deep infrared till deep UV. These high values are greater than those reported for popular UV optical application material such as borate crystals [61, 62] and could be attributed to the enhanced elastic anisotropy, along with the Jan–Teller distortions of ZnO_6 and TeO_6 octahedral [63].

4. Conclusion

The combination of variable composition screening and first principles techniques have uncovered two energetically, mechanically and dynamically stable ZnTe–O_2 phases under ambient pressure, namely the triclinic $P\bar{1}$-$Zn_2Te_2O_6$ and tetragonal $I\bar{4}$m2-$ZnTeO_4$. These phases have relatively wide G_0W_0 corrected band gap that broadens with more oxygen incorporation. Elevation of O is believed to promote covalent bonding via increased hybridization and sequentially improves the hardness. The high and sharp increase of absorption coefficient across UV range propel their suitability as UV absorber, which could possibly be merged with conventional solar panel to maximize light conversion. Interestingly, non-centrosymmetric $ZnTeO_4$ exhibits many of the desirable aspects in choosing exceptional nonlinear optical materials, as indicated by its high birefringence ($\Delta n \gg 0.08$), significant anisotropy and large SHG coefficients ($d_{14} = 9.84$ pm V^{-1} and $d_{36} = 2.33$ pm V^{-1} at static limit). The present theoretical study is expected to provide a better understanding of material parameters optimization via compositional tuning, required for synthesizing large single ZnTeO compound of optical quality.

Acknowledgments

We gratefully acknowledge the School of Physics, Universiti Sains Malaysia, for providing us with the computing resources to carry out the calculations shown in this study. Immense recognition must also be rendered to all Theory and Computational Laboratory (Physics School USM) personnel for their support and constructive inputs.

ORCID iDs

YeeHuiRobinChang https://orcid.org/0000-0002-4517-7059
Tiem Leong Yoon https://orcid.org/0000-0001-7334-710X

References

[1] Nordheim L 1931 Zur Elektronentheorie der Metalle *Ann. Phys.* **401** 607–40
[2] Thompson A G and Woolley J C 1967 Energy-gap variation in mixed III–V alloys *Can. J. Phys.* **45** 255–61
[3] Richardson D and Hill R 1972 The origins of energy gap bowings in substitutional semiconductor alloys *J. Phys. C: Solid State Phys.* **5** 8
[4] Walukiewicz W, Shan W, Yu K M III, Ager J W, Haller E E, Miotlowski I, Seong M J, Alawadhi H and Ramdas A K 2000 Interaction of localized electronic states with the conduction band: Band anticrossing in II–VI semiconductor ternaries *Phys. Rev. Lett.* **85** 1552–5

[5] Kondow M, Kitatani T, Nakatsuka S, Larson M C, Nakahara K, Yazawa Y, Okai M and Uomi K 1997 GaInNAs: a novel material for long-wavelength semiconductor lasers *IEEE J. Sel. Top. Quantum Electron.* **3** 719–30

[6] Kondow M, Kitatani T, Larson M C, Nakahara K, Uomi K and Inoue H 1998 Gas-source MBE of GaInNAs for long-wavelength laser diodes *J. Cryst. Growth* **188** 255–9

[7] López N, Reichertz L, Yu K M, Campman K and Walukiewicz W 2011 Engineering the electronic band structure for multiband solar cells *Phys. Rev. Lett.* **106** 028701

[8] Tanaka T, Yu K M, Levander A X, Dubon O D, Reichertz L A, Lopez N, Nishio M and Walukiewicz W 2011 Demonstration of $ZnTe_{1-x}O_x$ intermediate band solar cell *Japan. J. Appl. Phys.* **50** 082304

[9] Yu K M, Walukiewicz W, Wu J, Shan W, Beeman J W, Scarpulla M A, Dubon O D and Becla P 2003 Diluted II–VI oxide semiconductors with multiple band gaps *Phys. Rev. Lett.* **91** 246203

[10] Yu K M, Walukiewicz W, Wu J, Shan W, Beeman J W, Scarpulla M A, Dubon O D and Becla P 2004 Synthesis and optical properties of II–O–VI highly mismatched alloys *J. Appl. Phys.* **95** 6232

[11] Tanaka T, Kusaba S, Mochinaga T, Saito K, Guo Q, Nishio M, Yu K M and Walukiewicz W 2012 Molecular beam epitaxial growth and optical properties of highly mismatched $ZnTe_{1-x}O_x$ alloys *Appl. Phys. Lett.* **100** 011905

[12] Tanaka T, Nagao Y, Mochinaga T, Saito K, Guo Q, Nishio M, Yu K M and Walukiewicz W 2013 Molecular beam epitaxial growth of ZnCdTeO epilayers for intermediate band solar cells *J. Cryst. Growth* **378** 259–62

[13] Tang N, Hu Q, Ren A, Lia W, Liu C, Zhang J, Wu L, Li B, Zeng G and Hu S 2017 An approach to ZnTe:O intermediate-band photovoltaic materials *Sol. Energy* **157** 707

[14] Tanaka T, Yu K M, Okano Y, Tsutsumi S, Haraguchi S, Saito K, Guo Q, Nishio M and Walukiewicz W 2017 Properties of ZnTeO-based intermediate band solar cells with *n*-type ZnS layers *IEEE J. Photovolt.* **7** 1024

[15] Khelifi S, Mazari H, Belghachi A, Ameur K, Benamara Z, Mostefaoui M, Rouabhia A and Sahouane N 2017 Simulation analysis of intermediate band ZnTeo based thin film solar cell *J. Nanoelectron. Optoelectron.* **12** 460

[16] Lakehal B, Dibi Z and Lakhdar N 2017 New optimized intermediate band (IB) design to improve ZnTeO solar cell performances *J. Nano- and Electron. Phys.* **9** 6005

[17] Tanaka T, Saito K, Guo Q, Yu K M and Walukiewicz W 2018 Improved photovoltaic properties of ZnTeO-based intermediate band solar cells *Proc. SPIE* **10527** 105270P

[18] Ting M M, dos Reis R, Jaquez M, Dubon O D, Mao S S, Yu K M and Walukiewicz W 2015 Tunability of electronic band structures in ZnO-rich highly mismatched $ZnO_{1-x}Te_x$ alloys *Appl. Phys. Lett.* **106** 092101

[19] Mayer M A, Speaks D T M, Yu K M, Mao S S, Haller E E and Walukiewicz W 2010 Band structure engineering of $ZnO_{1-x}Se_x$ alloys *Appl. Phys. Lett.* **97** 022104

[20] Nie K Y *et al* 2018 Tailored emission properties of ZnTe/ZnTe:O/ZnO core-shell nanowires coupled with an al plasmonic bowtie antenna array *ACS Nano* **12** 7327

[21] Zhao L, Fan F Y, Cai Y Y, Tian C Y, Li Y Y and Lin S B 2018 Synthesis and luminescence properties of red-emitting Sr_2ZnTeO_6: Eu^{3+} phosphors *Chin. J. Lumin.* **39** 1193

[22] Zerroug S, Gueddim A, Ajmal Khan M and Bouarissa N 2013 *Ab initio* study of structural parameters and optical properties of $ZnTe_{1-x}O_x$ *Superlattices Microstruct.* **53** 155

[23] Silambarasan A, Rao E N, Rao S V, Rajesh P and Ramasamy P 2016 Bulk growth, crystalline perfection and optical characteristics of inversely soluble lithium sulfate monohydrate single crystals grown by the conventional solvent evaporation and modified Sankaranarayanan–Ramasamy method *CrystEngComm* **18** 2072–80

[24] Bensebaa F 2013 Chapter 7—optoelectronics *Interface Sci. Technol.* **19** 429–79

[25] Oganov A R and Glass C W 2006 Crystal structure prediction using evolutionary algorithms: principles and applications *J. Chem. Phys.* **124** 244704

[26] Lyakhov A O, Oganov A R, Stokes H and Zhu Q 2013 New developments in evolutionary structure prediction algorithm USPEX *Comput. Phys. Commun.* **184** 1172–82

[27] Hohenberg P and Kohn W 1964 Inhomogeneous electron gas *Phys. Rev.* **136** B864

[28] Gonze X, Ghosez Ph and Godby R W 1997 Density functional theory of polar insulators *Phys. Rev. Lett.* **27** 294

[29] Kresse G and Furthmüller J 1996 Efficient iterative schemes for *ab initio* total-energy calculations using a plane-wave basis set *Phys. Rev.* B **54** 11169

[30] Kresse G and Furthmüller J 1996 Efficiency of *ab initio* total energy calculations for metals and semiconductors using a plane-wave basis set *Comput. Mater. Sci.* **6** 15–50

[31] Perdew J and Wang Y 1992 Accurate and simple analytic representation of the electron-gas correlation energy *Phys. Rev.* B **45** 13244

[32] Hamann D R, Wu X, Rabe K M and Vanderbilt D 2005 Metric tensor formulation of strain in density-functional perturbation theory *Phys. Rev.* B **71** 035117

[33] Gonze X *et al* 2005 A brief introduction to the ABINIT software package *Z. Kristallogr.* **220** 558–62

[34] Gonze X *et al* 2009 ABINIT: first-principles approach of materials and nanosystem properties *Comput. Phys. Commun.* **180** 2582–615

[35] Perdew J P, Burke K and Ernzerhof M 1996 Generalized gradient approximation made simple *Phys. Rev. Lett.* **77** 3865

[36] Haynes W M 2011 *CRC Handbook of Chemistry and Physics* 92nd edn (Boca Raton, FL: CRC Press)

[37] Kittel C 2004 *Introduction to Solid State Physics* 8th edn (New York: Wiley)

[38] Kumar V, Kumar V and Dwivedi D K 2012 Growth and characterization of zinc telluride thin films for photovoltaic applications *Phys. Scr.* **86** 015604

[39] Nukui A, Todoroki S, Miyata M and Bando Y 2002 *In situ* high-temperature x-ray observations of crystallization of zinc tellurite glass *Mater. Trans.* **43** 3

[40] Nabetani Y, Okuno T, Aoki K, Kato T, Matsumoto T and Hirai T 2006 Epitaxial growth and optical investigations of ZnTeO alloys *Phys. Status Solidi* a **203** 2653–7

[41] Lyakhov A and Oganov A 2011 Evolutionary search for superhard materials: methodology and applications to forms of carbon and TiO_2 *Phys. Rev.* B **84** 092103

[42] Lekse J W, Moreau M A, McNerny K L, Yeon J, Halasyamani P S and Aitken J A 2009 Second-harmonic generation and crystal structure of the diamond-like semiconductors Li_2CdGeS_4 and Li_2CdSnS_4 *Inorg. Chem.* **48** 7516–8

[43] Brant J A, Clark D J, Kim Y S, Jang J I, Zhang J-H and Aitken J A 2014 Li_2CdGeS_4: a diamond-like semiconductor with strong second-order optical nonlinearity in the infrared and exceptional laser damage threshold *Chem. Mater.* **26** 3045–8

[44] Mouhat F and Coudert F X 2014 Necessary and sufficient elastic stability conditions in various crystal systems *Phys. Rev.* B **90** 224104

[45] Sin'ko G V and Smirnov N A 2005 Relative stability and elastic properties of hcp, bcc, and fcc beryllium under pressure *Phys. Rev.* B **71** 214108

[46] Gaillac R, Pullumbi P and Coudert F 2016 ELATE: an open-source online application for analysis and visualization of elastic tensors *J. Phys.: Condens. Matter* **28** 275201
[47] Greaves G N, Greer A L, Lakes R S and Rouxel T 2011 Poisson's ratio and modern materials *Nat. Mater.* **10** 823–37
[48] Frantsevich I N, Voronov F F and Bokuta S A 1990 *Elastic Constants and Elastic Moduli of Metals and Insulators Handbook 1982* (Kiev: Naukova Dumka) pp 60–180
[49] Shivakumar I R and Martin O S 2008 Universal elastic anisotropy index *Phys. Rev. Lett.* **101** 055504
[50] Sakhya A P, Rai D P, Sheikh M S, Mukherjee M, Dutta A and Sinha T P 2017 Origin of the optical anisotropy and the electronic structure of Ru-based double perovskite oxides: DFT and XPS studies *RSC Adv.* **7** 43531–9
[51] Sharma S and Ambrosch-Draxl C 2004 Second-harmonic optical response from first principles *Phys. Scr.* **109** 128–34
[52] Sipe J E and Ghahramani E 1993 Nonlinear optical response of semiconductors in the independent-particle approximation *Phys. Rev.* B **48** 11705
[53] Chang Y H R, Yoon T L and Lim T L 2016 *Ab initio* computations of the linear and nonlinear optical properties of stable compounds in Al–In–N system *Curr. Appl. Phys.* **16** 1277–83
[54] Chang Y H R, Yoon T L, Lim T L, Koh P W and Tuh M H 2019 Frequency dependent linear and nonlinear optical properties of compositionally tuned inorganic CsSnX (X = Br, I) composites *J. Alloys Compd.* **779** 497–504
[55] Penn D R 1962 Wave-number-dependent dielectric function of semiconductors *Phys. Rev.* **128** 2093–7
[56] Bian Q, Yang Z, Dong L, Pan S, Zhang H, Wu H, Yu H, Zhao W and Jing Q 2014 First principle assisted prediction of the birefringence values of functional inorganic borate materials *J. Phys. Chem.* C **118** 25651–7
[57] Kleinman D A 1962 Nonlinear dielectric polarization in optical media *Phys. Rev.* **126** 1977
[58] Chen C T, Lu J H, Togashi T, Suganuma T, Sekikawa T, Watanabe S, Xu Z Y and Wang J Y 2002 Second-harmonic generation from a $KBe_2BO_3F_2$ crystal in the deep ultraviolet *Opt. Lett.* **27** 637–9
[59] Wu B C, Tang D Y, Ye N and Chen C T 1996 Linear and nonlinear optical properties of the $KBe_2BO_3F_2$ crystal *Opt. Mater.* **5** 105–9
[60] Chen C T, Wang G L, Wang X Y and Xu Z Y 2009 Deep-UV nonlinear optical crystal $KBe_2BO_3F_2$—discovery, growth, optical properties and applications *Appl. Phys. B: Lasers Opt.* **97** 9 − 25
[61] Reshak A H and Auluck S 2017 Two haloid borate crystals with large nonlinear optical response *Phys. Chem. Chem. Phys.* **19** 18416–25
[62] Zhang M *et al* 2014 Linear and nonlinear optical properties of $K_3B_6O_{10}Br$ single crystal: experiment and calculation *J. Phys. Chem.* C **118** 11849–56
[63] Shiv Halasyamani P 2004 Asymmetric cation coordination in oxide materials: influence of lone-pair cations on the intra-octahedral distortion in d^0 transition metals *Chem. Mater.* **16** 3586–92